small structures
www.small-structures.com

M(III) Site-Driven Structural Engineering on Lead-Free Layered Double Perovskite Nanocrystals with Enhanced Photoelectrochemical Activity

*Yukta, Sunardi Rahman, Qi Shi, Tarek Al Said, Sri Kasi Matta, Tianyi Hu, Weimin Wang, Amanda Opis-Basilio, Kallol Ray, Kimberly A. Dick, Tönu Pullerits, and Maning Liu**

Over the past decade, organic–inorganic hybrid perovskites have revolutionized next-generation semiconductors, driving unprecedented advancements in cost-effective optoelectronics. While lead-based perovskite semiconductors exhibit exceptional optoelectronic properties, their inherent toxicity and vulnerability to environmental degradation remain significant barriers to widespread commercialization. Vacancy-ordered layered double perovskites (LDPs) offer a viable alternative with direct bandgaps, reduced toxicity, superior stability, and tunable properties, while their divalent and trivalent cation integration enables precise control over electronic and photophysical characteristics for efficient optoelectronics. Herein, the M(III) cation site within the previously reported $Cs_4CoIn_2Cl_{12}$ LDP system by substituting In^{3+} with Bi^{3+} and Sb^{3+} is systematically modified, achieving the first-ever colloidal synthesis of $Cs_4CoBi_2Cl_{12}$ and $Cs_4CoSb_2Cl_{12}$ nanocrystals (NCs). A detailed investigation of their optoelectronic properties reveals significant structural distortions induced by different M(III) cations. Stability assessments demonstrate that $Cs_4CoSb_2Cl_{12}$ exhibits exceptional air and compositional stability, maintaining its compositional integrity for over 100 days under ambient conditions. Furthermore, the photoelectrochemical (PEC) performance of these NCs in benzoquinone oxidation is explored, identifying $Cs_4CoBi_2Cl_{12}$ as the most efficient candidate, with a stable photoresponse and enhanced photocurrent generation. Transient absorption studies further confirm that $Cs_4CoBi_2Cl_{12}$ sustains the largest self-trapped exciton population and longest half-lifetime, highlighting its potential for sustainable, high-performance PEC devices.

1. Introduction

In recent years, lead-based halide perovskite nanocrystals (NCs) have garnered significant attention for their potential in advanced optoelectronic applications, attributed to the exceptional combination of their unique optical and electronic properties.[1–5] Despite their remarkable optoelectronic properties and high photoluminescence quantum yields (PLQYs), their susceptibility to environmental degradation, particularly in the presence of moisture and polar solvents, coupled with the toxicity of Pb^{2+} ions, poses major roadblocks to their commercialization.[6,7] To address these challenges, alternative metal cations can be successfully substituted for Pb while maintaining the material's distinctive characteristics to make environmentally benign perovskites.[8–11] The substitution of Pb^{2+} cations through homovalent (Sn^{2+} and Ge^{2+}) and heterovalent (Sb^{3+}, Bi^{3+}) counterparts is a fruitful strategy to reduce toxicity as well as to maintain the distinctive properties of perovskites.[12,13] In the category of heterovalent cation substitution, the <111>-oriented vacancy-ordered layered perovskites with the general formula $A_{n+1}B_nX_{3n+3}$ (where $n > 2$, A—organic/inorganic metal cation, X—halide anions) and B

Yukta, S. Rahman, T. Hu, K. A. Dick, M. Liu
Centre for Analysis and Synthesis
Department of Chemistry
Lund University
P.O. Box 124, 221 00 Lund, Sweden
E-mail: maning.liu@chem.lu.se

The ORCID identification number(s) for the author(s) of this article can be found under https://doi.org/10.1002/sstr.202500179.

DOI: 10.1002/sstr.202500179

Yukta, S. Rahman, K. A. Dick, M. Liu
Wallenberg Initiative Materials Science for Sustainability
Department of Chemistry
Lund University
Lund 221 00, Sweden

Yukta, S. Rahman, Q. Shi, T. Hu, K. A. Dick, T. Pullerits, M. Liu
NanoLund
Lund University
Professorsgatan 1, 223 63 Lund, Sweden

Q. Shi, T. Pullerits
Chemical Physics
Department of Chemistry
Lund University
Kemicentrum Naturvetarevägen 16, 223 62 Lund, Sweden

consisting of a mixture of different cations belong to a subclass of heterometallic layered double perovskites (LDPs).[14,15] These materials, represented by the general formula $A_4M(II)M(III)_2X_{12}$, constitute a novel class of lead-free perovskites characterized by a distinctive layered architecture. Structurally, the perovskite consists of one layer of $[M(II)X_6]^{4-}$ octahedral units, flanked by two adjacent corner-sharing $[M(III)X_6]^{3-}$ octahedral units, with metal cations (Cs^+) occupying the interstitial sites.[16,17] Notably, the direct bandgap nature (almost comparable to traditional 3D $CH_3NH_3PbI_3$), superior structural stability and versatility, and reduced toxicity distinguish these materials from conventional indirect-bandgap double perovskites and low-dimensional $A_3B_2X_9$ vacancy-ordered perovskites.[18]

Theoretical predictions suggest that LDPs can adopt several stable structural configurations, including Fd3m and C2/m space groups, by incorporating diverse M(II) cations such as Cu^{2+}, Zn^{2+}, Mn^{2+}, Cd^{2+}, Co^{2+}, and Sn^{2+}, along with M(III) cations like In^{3+}, Bi^{3+}, and Sb^{3+}, and halides (Cl, Br, I).[19] The pioneering synthesis of layered halide double perovskites was reported by Solis-Ibarra and coworkers, who developed $Cs_4CuSb_2Cl_{12}$ microcrystalline powder with a direct bandgap of 1.02 eV.[16] Building on this foundation, a detailed investigation into $Cs_4CuSb_2Cl_{12}$ perovskites was done, leading to significant advancements. Most significantly, Chen et al. successfully synthesized colloidal $Cs_4CuSb_2Cl_{12}$ NCs via a conventional hot-injection method, systematically analyzing their photophysical and structural properties. Later on, the promising photoelectrochemical (PEC) response from these NCs was predicted, and an ultrafast photodetector with a narrow bandwidth (≈10 GHz) and an ultrashort decay lifetime of 150 ps was fabricated.[20] Interestingly, versatile LDPs are also well suited for energy conversion applications, as Huang et al. successfully demonstrated the efficient photocatalytic dehydrogenation of ammonia borane using $Cs_4CuSb_2Cl_{12}$ perovskite NCs.[21] Subsequently, Liu et al. explored the incorporation of In^{3+} as a substitute for Sb^{3+} and achieved the first colloidal wet precursor synthesis of $Cs_4CuIn_2Cl_{12}$ NCs, demonstrating an enhanced PLQY of 1.70%. Moreover, they discovered that moisture exposure induces a morphological transformation in $Cs_4CuIn_2Cl_{12}$ NCs, triggering a structural shift from 3D nanocubes to 2D nanoplatelets. This transition effectively converts nonradiative dark states into radiative self-trapped exciton (STE) relaxation, offering a novel strategy for tuning optoelectronic properties in perovskite materials.[22] Successively, Caruso et al. expanded the LDP family by synthesizing $Cs_4ZnSb_2Cl_{12}$ colloidal NCs, demonstrating precise control over their size and morphology. This tunability enabled a comprehensive investigation into the correlation between structural parameters and optoelectronic properties. Accordingly, shape-dependent photocatalytic activity was observed, with 9.7 nm nanoplatelets exhibiting exceptional efficiency in photocatalytic toluene oxidation.[23] These nanostructures facilitated the conversion of toluene to benzaldehyde with a remarkable reaction yield of 1893 μmol g^{-1} h^{-1}, significantly surpassing that of bulk counterparts synthesized without morphological control. In a recent study, Liu et al. advanced the lattice engineering strategies to synthesize $Cs_4M(II)In_2X_{12}$ NCs by systematically varying the M(II) cation from Cu^{2+} (as control) to Zn^{2+} and to Co^{2+}. Their findings revealed significant lattice distortions in these perovskites, leading to an enhanced formation of STEs, particularly in $Cs_4ZnIn_2Cl_{12}$ NCs. Surprisingly, Zn^{2+}-based NCs exhibited an impressive PLQY of 11.4%, attributed to the optimized lattice deformation energy. In both $Cs_4CoIn_2X_{12}$ and $Cs_4ZnIn_2X_{12}$ systems, the deformation energy remained within an optimal range, facilitating efficient radiative recombination of STEs. This study underscores the critical role of lattice distortions and cation engineering in tuning the optoelectronic properties of LDPs for next-generation energy applications.[24]

Therefore, the strategic co-integration of divalent and trivalent metal cations broadens the compositional landscape of LDPs, enabling the design of novel materials with precisely tunable structural and photo-induced charge transfer properties.[19,25] In this work, we in turn systematically modified the M(III) cation site based on the previously reported $Cs_4CoIn_2Cl_{12}$ class of LDPs by substituting In^{3+} with Bi^{3+} and Sb^{3+}, respectively, leading to the first-ever successful synthesis of $Cs_4CoBi_2Cl_{12}$ and $Cs_4CoSb_2Cl_{12}$ colloidal NCs. We conducted a comprehensive investigation into the optoelectronic properties of these NCs, analyzing the structural distortions induced by different M(III) cations. Furthermore, we assessed the air and compositional stability of all three NCs, revealing that $Cs_4CoSb_2Cl_{12}$ retained its stability for over 100 days under ambient conditions. Our study also demonstrates that STEs arise due to the variable degree of lattice distortion in all three NCs; however, they contribute to photoluminescence (PL) enhancement only in $Cs_4CoIn_2Cl_{12}$ NCs. We fabricated the PEC cells by employing the NCs as the photoanode for realizing the PEC oxidation reaction. The $Cs_4CoBi_2Cl_{12}$ NCs exhibited the highest photocurrent density of 150 μA cm^{-2}—a 1.5-fold increase compared to the reference case of $Cs_4CoIn_2Cl_{12}$. Our transient absorption measurements further confirm that $Cs_4CoBi_2Cl_{12}$ NCs feature the largest population of photogenerated STE states along with the longest half-lifetime compared to the other two cases, clearly emphasizing the big potential of these types of lead-free LDP NCs in eco-friendly and high-performance PEC applications.

2. Results and Discussion

2.1. Optical and structural properties of as-synthesized Co-based LDP NCs

In the colloidal synthesis, Bi^{3+} and Sb^{3+} were specifically introduced as alternatives for In^{3+} at the M(III) site, that is, $Cs_4CoIn_2Cl_{12}$ NCs

T. A. Said
Helmholtz-Zentrum Berlin für Materialien und Energie
Hahn-Meitner-Platz 1, 14109 Berlin, Germany

S. K. Matta
School of Chemistry and Physics
Queensland University of Technology
Brisbane, QLD 4000, Australia

W. Wang
MAX IV Laboratory
Fotongatan 2, 224 84 Lund, Sweden

A. Opis-Basilio, K. Ray
Institut für Chemie
Humboldt-Universität zu Berlin
Brook-Taylor-Str. 2, 12489 Berlin, Germany

as control, leading to the formation of two new colloidal $Cs_4CoBi_2Cl_{12}$ and $Cs_4CoSb_2Cl_{12}$ NCs in this work.[24] Furthermore, we hypothesized that the changes in optoelectronic properties could mainly result from the effective structural (lattice) engineering of the M(III) site cations in this type of LDP structure. The size-tunable colloidal $Cs_4CoM(III)_2Cl_{12}$ NCs were synthesized by employing a modified hot injection method (see the detailed synthetic procedure in the Supporting Information (SI)).[24] Typically, the targeted NCs were prepared through the rapid ionic metathesis reaction, which is initiated by the swift injection of a chlorine precursor into a mixture of metal cation precursor at high temperatures, that is, 180 °C for In^{3+} and Bi^{3+} and 230 °C for Sb^{3+}. A schematic illustration of hot-injection synthesis route for $Cs_4CoM(III)_2Cl_{12}$ (M = In, Bi, Sb) NCs is provided in **Figure 1**a, outlining the sequential precursor injection process under inert conditions. The as-synthesized $Cs_4CoM(III)_2Cl_{12}$ NCs, where M(III) corresponds to In^{3+}, Bi^{3+}, and Sb^{3+}—yielding the compositions $Cs_4CoIn_2Cl_{12}$, $Cs_4CoBi_2Cl_{12}$, and $Cs_4CoSb_2Cl_{12}$, respectively—are hereafter referred to as CoIn, CoBi, and CoSb. Figure 1b presents a schematic illustration of the alternative octahedral stacking in a typical $Cs_4CoM(III)_2Cl_{12}$-layered structure. As the M(III) site is substituted from pristine In^{3+} to Bi^{3+} and to Sb^{3+}, the color of the NCs changes from turquoise blue to light blue and then to dark green, indicating a corresponding change in their bandgap. We first investigated the optical properties of as-synthesized $Cs_4CoM(III)_2Cl_{12}$ NCs. The absorption spectra of CoIn NCs exhibited a distinct excitonic peak in the ultraviolet region, occurring at wavelengths shorter than 325 nm (Figure 1c). In contrast, the excitonic absorption peak of CoBi NCs was redshifted to 366 nm, while the CoSb NCs displayed two excitonic peaks within the range of 300–450 nm. Additionally, a broad absorption band spanning 600–720 nm was observed, characterized by multiple overlapping peaks. This spectral feature corresponds to the presence of $[CoCl_4]^{2-}$ tetrahedral ions, which arise due to metal-to-ligand charge transfer while involving weak *d–d* electronic transitions.[26] The broad absorption band indicative of $[CoCl_4]^{2-}$ formation was consistently observed in both CoIn- and CoSb-based NCs but was clearly absent in the CoBi variant. This indicated the variations in the local ligand field environment and electronic interactions governed by the trivalent metal cations (In^{3+}, Sb^{3+}, Bi^{3+}), further suggesting that in the CoBi system, cobalt ions may adopt an alternative coordination geometry or experience distinct electronic coupling effects that inhibit the formation of $[CoCl_4]^{2-}$. The optical bandgap of the NCs was determined using the Tauc plot by extrapolating the linear region of the $(\alpha h\nu)^2$ versus $h\nu$ curve to its intersection with the photon energy axis, where α represents the absorption coefficient and $h\nu$ denotes the photon energy.[27] Sequentially, the bandgap of CoIn NCs was calculated as 3.67 eV, whereas a reduction in bandgap was observed for CoBi (3.23 eV) and CoSb (2.88 eV) NCs, respectively (Figure 1d). This indicates a systematic reduction in bandgap energy by the substitution of Bi^{3+} and Sb^{3+} for reference In^{3+} at the M(III) site, possibly due to the enhanced spin-orbit coupling and changes in the electronic structure of perovskite NCs.[28] These effects can collectively lead to the stabilization of conduction band states to reduce energy gaps and the redshifted optical absorption in the $Cs_4CoM(III)_2Cl_{12}$ NC system.[28–30] The X-ray diffraction (XRD) patterns of $Cs_4CoM(III)_2Cl_{12}$ NCs are presented in Figure 1e, providing insight into their crystalline structure. Here, the experimental XRD patterns were compared with the diffraction pattern of the reference $Cs_4CuSb_2Cl_{12}$ (CuSb) material (ICSD 243 918) as well as the individually calculated patterns for each composition.[20] When compared with characteristic CuSb crystalline diffraction patterns, all three NC systems exhibited distinct peaks at ≈24°, 25°, 33.4°, 34.8°, 41.6°, and 43.7°, which correspond to the $(\bar{3}11)$, (020), $(40\bar{4})$, (222), $(\bar{4}22)$, and (511) lattice planes, respectively. These reflections are characteristic of a LDP structure that features the distorted $[M(II)Cl_6]$ octahedra. Among the three compositions, CoSb exhibited the highest degree of agreement with the characteristic XRD pattern of reference CuSb. In contrast, CoIn and CoBi NCs showed noticeable deviations in their diffraction patterns. Specifically, the $(\bar{3}11)$and (020) reflections merge into a single broad peak, while the $(40\bar{4})$ and $(\bar{4}22)$ reflections exhibit an upward shift. These observations suggest subtle lattice distortions and structural variations within these compositions. Furthermore, the XRD patterns for the individual CoBi and CoSb systems (drop-casted thin films and powder precipitates), overlaid with their respective simulated patterns, are provided in the SI. We attempted to simulate the single-crystal XRD structures for the NCs. The major characteristic peaks of each NC are individually marked (Figure S1, Supporting Information). The simulated patterns exhibited almost similar XRD profiles for both the NCs powder, with slight variations in peak intensity. Notably, the experimental CoSb NCs pattern similarly showed the highest agreement with the simulated data, whereas CoBi exhibited slight peak broadening and an upward shift in diffraction peaks. The lattice parameters calculated from the simulated patterns are consistent across both NCs, with values of $a = 7.543$ Å, $b = 7.543$ Å, $c = 13.085$ Å, $\alpha = \beta = 106.85°$, and $\gamma = 59.55°$. The simulated structural analysis revealed significant distortions in both inserted $[CoCl_6]$ and two adjacent $[M(III)Cl_6]$ octahedra for all three NCs. Specifically, the Co—Cl bond distances were measured as 2.269 Å (axial) and 3.047 Å (equatorial) for CoIn, 2.359 Å (axial) and 2.482 Å (equatorial) for CoSb, and 2.359 Å (axial) and 2.521 Å (equatorial) for CoBi. This variation is a clear indication of Jahn–Teller distortion in the Co^{2+} ion,[31] providing additional (though indirect) evidence of the oxidation state of the cobalt atom (Figure S2a, Supporting Information). The Jahn–Teller distortion in the $[CoCl_6]$ octahedra can possibly contribute to the formation of STEs in these LDP NCs.[22,24,32] In addition, the steady-state photoluminescence (PL) spectra of the NCs, shown in Figure S3a, Supporting Information, were recorded in hexane.

After correction with the absorptivity at the excitation wavelength (first excitonic peak in each case), the highest PL intensity peak was observed at 403 nm for CoIn, while the redshifted low-intensity emission peaks were noted at 416 and 419 nm, respectively, for CoSb and CoBi (see Figure S3b, Supporting Information**)**. Additionally, the PL spectra for all the NCs demonstrated broad asymmetric profiles (full width at half maximum 43 nm for CoIn, 48.6 nm for CoBi, and 46.7 nm for CoSb) with a long tail and feeble intensity hump-like features toward 700 nm, indicating the presence of multiple emission pathways. The broad absorption features in LDPs are primarily attributed to the STE emissions.[24,33,34] We also carried out the time-resolved PL measurements and extracted the carrier lifetimes (Figure S3c, Supporting Information). The PL decays were found to follow the

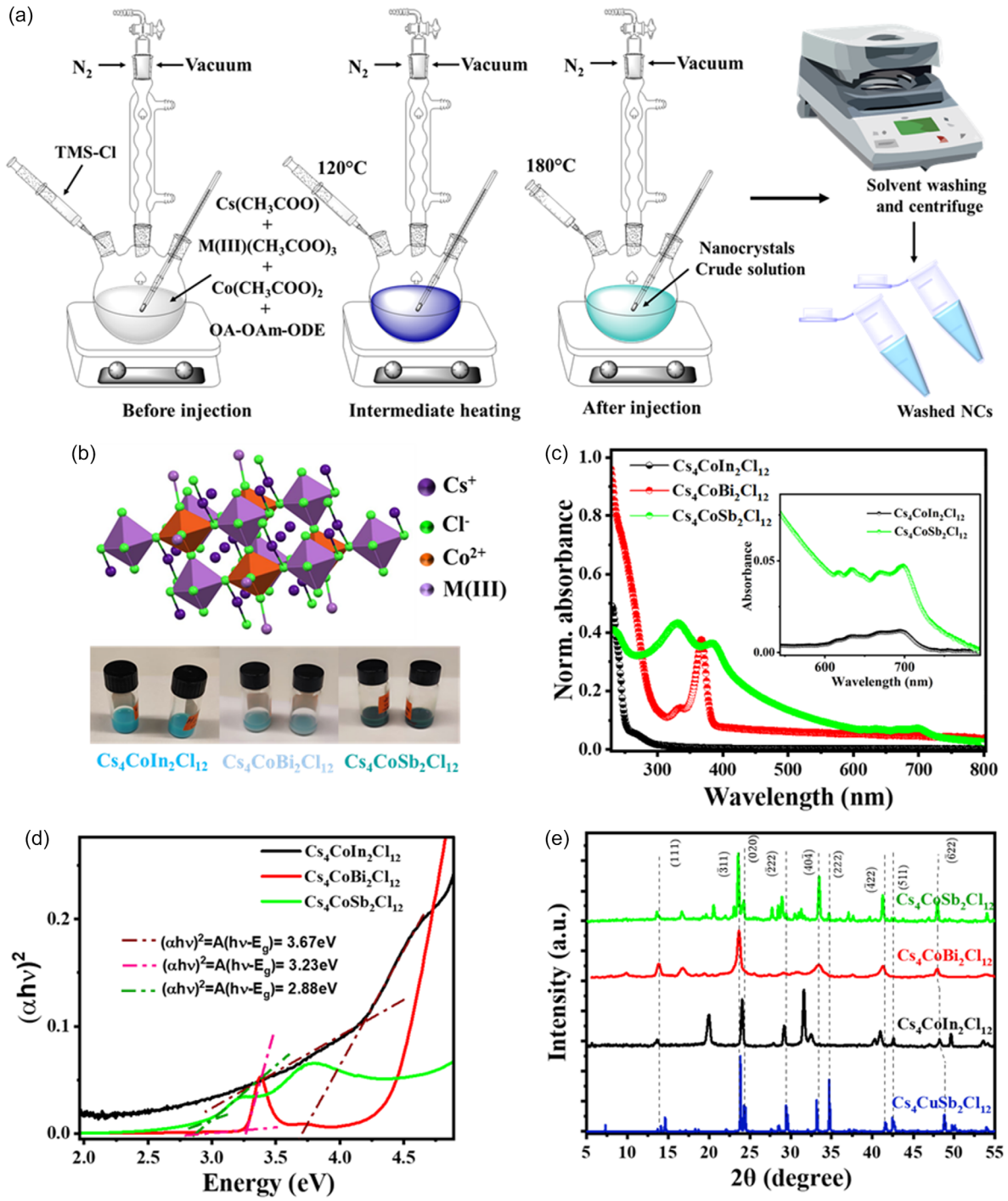

Figure 1. a) Schematic illustration of the hot-injection synthetic route for $Cs_4CoM(III)_2Cl_{12}$ (M = In, Bi, Sb) NCs. b) Schematic representation of expected structural packing of LDP $Cs_4CoM(III)_2Cl_{12}$. Bottom photographic representation of NC suspensions highlights distinct color variations for different M(III) cations (In^{3+}, Bi^{3+}, Sb^{3+}). c) Normalized UV–visible spectra of CoIn, CoBi, and CoSb NCs dispersed in hexane; zoomed-out inset image for wavelength 600–750 nm showing the presence of $[CoCl_4]^{2-}$ tetrahedral ions. d) Tauc plots showing clear bandgap variation for $Cs_4CoM(III)_2Cl_{12}$ NCs with diverse M(III) cations (In^{3+}, Bi^{3+}, Sb^{3+}). e) Comparison of XRD patterns of as-synthesized $Cs_4CoM(III)_2Cl_{12}$ NCs with reported characteristic $Cs_4CuSb_2Cl_{12}$ perovskite as the reference pattern.

bi-exponential decay kinetics (see Table S1, Supporting Information), confirming the presence of multiple recombination pathways. Interestingly, all three NCs demonstrated almost identical first decay components before the PL intensity decreased to be half (50%) of peak intensity, hinting that the number of surface or shallow traps could be similar among the three NCs, whereas

their deep or bulk traps indeed differ that causes the moderate deviation in their average lifetimes in a range of ≈183 to 297 ps.

Furthermore, to determine the stoichiometry of as-synthesized NCs, energy-dispersive X-ray spectroscopy (EDS) analysis was performed. **Figure 2**a–c presents the field emission scanning electron microscopy (FESEM) images of as-synthesized NCs. Accordingly, the EDS analysis was conducted to verify the elemental composition of all three LDP NCs. The atomic weight ratio calculations confirmed that all these NCs adhered to the nominal stoichiometric ratio of 4:1:2:12 for Cs, Co, M(III), and Cl, respectively (see corresponding EDS spectra in Figure S4a–c, Supporting Information). The atomic weight percentage values for CoIn, CoBi, and CoSb NCs are summarized in Table S2, Supporting Information, further validating the compositional accuracy. The EDS elemental mapping images presented in Figure S4d–f, Supporting Information, demonstrated a uniform spatial distribution of Cs, Co, M(III), and Cl throughout the NCs, indicating homogeneous composition across the samples. Additionally, X-ray photoelectron spectroscopy (XPS) was used to verify the valence states of the metal ion centers, specifically $M(III)^{3+}$ and Co^{2+}, and to investigate the bonding environment of Cl, Cs, and Co upon substitution of In^{3+} with Bi^{3+} and Sb^{3+} in the LDP structure. For CoIn NCs, two distinct peaks appeared at 446.6 and 454.2 eV, corresponding to In 3 $d_{5/2}$ and 3 $d_{3/2}$ (i.e., two binding orbitals of In^{3+} ions), respectively. Instead, the CoBi NCs peaks at 160.5 and 165.9 eV were assigned to Bi^{3+} 4$f_{7/2}$ and 4$f_{5/2}$ orbitals, while the CoSb NCs exhibit binding energy peaks at 531.9 and 540.7 eV, attributed to Sb^{3+} 3 $d_{5/2}$ and 3 $d_{3/2}$ orbitals, respectively. The XPS data confirmed the successful incorporation of Bi and Sb into the NC lattices (Figure S5a–f, Supporting Information). Additionally, the Cs 3*d* binding energy underwent slight variations following the substitution of In with Bi and Sb. Given that the ionic radius of In^{3+} is comparable to that of Sb^{3+}, only a negligible shift for Cs was observed in the

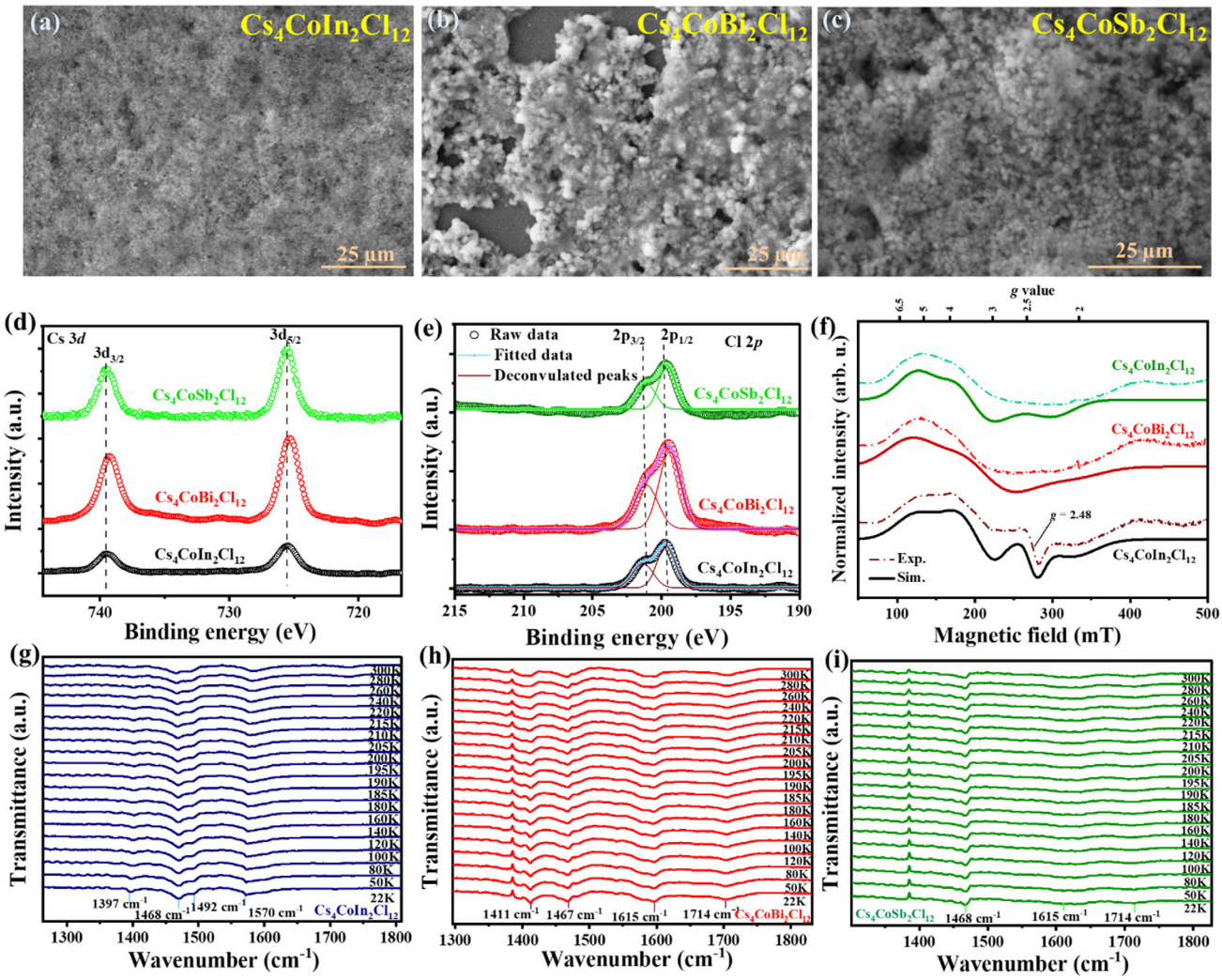

Figure 2. a–c) FESEM images of as-synthesized NCs thin films, that is, $Cs_4CoM(III)_2Cl_{12}$, M(III) cations = In^{3+}, Bi^{3+}, Sb^{3+} used for the EDS measurements. High-resolution XPS spectra for d) Cs 3*d* and e) Cl 2*p* states for $Cs_4CoM(III)_2Cl_{12}$ NCs. f) X-band EPR spectra of $Cs_4CoM(III)_2Cl_{12}$ NCs dispersions at a temperature of 12.5 K, recorded with a modulation frequency of 10 G and a microwave power of 0.25 mW. g–i) Temperature-dependent infrared spectra of $Cs_4CoM(III)_2Cl_{12}$ NCs in a range of 20–300 K.

case of CoSb NCs. However, when Bi^{3+} is introduced in place of In^{3+}, a shift of ≈0.20 eV occurred, indicating that Cs experiences a more electronegative environment due to local lattice strain induced by differences in the ionic radii of In^{3+}, Bi^{3+}, and Sb^{3+} (Figure 2d).[35] For Cl, two peaks were recorded at 199.6 and 201.3 eV, corresponding to Cl $2p_{3/2}$ and $2p_{1/2}$ orbitals, respectively, in CoIn NCs. These peaks shift by ≈0.18 eV in CoSb NCs and 0.27 eV in CoBi NCs, suggesting that chloride ions experience different chemical environments. This indicated stronger bonding of Cl with Bi and Sb compared to In in NCs, likely due to variations in bond lengths, which was consistent with the bond length calculations from the structural simulation (Figure S2b, Supporting Information). The observed shift implied an increase in covalency from the substitution of In with Bi and Sb in the as-synthesized perovskite NC lattices (Figure 2e).[28,36] While the binding energy shift for Cs was minimal, the shift for Cl was more pronounced. Interestingly, a weak-intensity and noisy XPS spectrum for Co was detected at the expected divalent state, with the $2p_{3/2}$ peak appearing at 783.6 eV (Figure S6, Supporting Information). However, due to the small ratios of signal to noise, precise quantification of the binding energy shift remained challenging, possibly due to the lower concentration of Co on the surface in a depth of ≈7 nm.[37] To confirm the presence of Co^{2+} in all three NCs, electron paramagnetic resonance (EPR) measurements were conducted. As shown in Figure 2f, the X-band EPR spectra of CoIn, CoSb, and CoBi NCs recorded at 12.5 K exhibit a resonance peak centered around 120 mT ($g \approx 4$), a clear characteristic of high-spin (HS, $S = 3/2$) Co(II). Additionally, a prominent signal at 280 mT ($g \approx 2.5$) was observed in CoIn NCs, indicative of a low-spin (LS, $S = 1/2$) Co(II) species. Closer examination reveals a shoulder around 180 mT, most pronounced in the CoIn spectrum but also present in the other compositions. This suggested the presence of an additional HS Co(II) species in all NCs, exhibiting slightly different magnetic parameters, likely due to variations in local coordination environments. As the temperature increases, the signal amplitudes decrease due to fast relaxation effects (Figure S7, Supporting Information). HS Co(II) typically exhibited significant zero-field splitting (ZFS), which separates the two Kramers' doublets ($m_S = \pm 1/2$ and $m_S = \pm 3/2$), ensuring that only the lowest doublet was populated at 12.5 K.[38] Nevertheless, the photon energy used in X-band EPR (≈0.3 cm^{-1}) is insufficient to induce transitions between these doublets. Therefore, the observed spectral features were attributed to transitions within the ground-state doublets, confirming the valence state of Co^{2+} ions in the as-synthesized NCs.

Figure 2g–i presents the temperature-dependent infrared spectra of CoIn, CoSb, and CoBi NCs over the 20–300 K range, providing insights into structural distortions induced by the substitution of In^{3+} with Bi^{3+} and Sb^{3+} in $Cs_4CoM(III)_2Cl_{12}$ NCs. The spectral region between 1300 and 1900 cm^{-1} primarily corresponded to molecular vibrations of the stabilizing ligands, that is, oleic acid (OA) and oleyl amine (OAm), while lattice vibrations of the NCs are expected to appear at lower frequencies in the far-infrared region. A characteristic vibrational band at 1468 cm^{-1}, observed in all NCs, was attributed to the C-H bending mode of methylene groups in the alkane chains of OA and OAm ligands.[39] Additional C-H vibrational bands appeared at 1397 and 1492 cm^{-1} in CoIn NCs and shifted to 1411 cm^{-1} in CoBi NCs, indicating subtle alterations in ligand binding interactions due to the lattice strain. Furthermore, the N^+-H bending vibrations of OAm, which reflected Cl-H hydrogen bonding interactions at the NC surface, exhibited a progressive increase in frequency from 1570 cm^{-1} in CoIn to 1615 cm^{-1} in CoSb.[39,40] This shift suggested an enhancement in hydrogen bond strength upon In substitution while implying modifications in the local coordination environment of Cl due to the structural rearrangement. The carboxyl (C═O) stretching mode of OA appeared between 1704 and 1714 cm^{-1} in CoSb and CoBi NCs but was absent in CoIn NCs. Interestingly, in CoSb NCs, this band was broader and redshifted compared to CoBi NCs, indicating weaker and less defined hydrogen bonding of carboxyl groups with the NC surface. These spectral variations clarified the distinct differences in lattice distortions and surface interactions among all three NCs. These deviations are plausibly attributed to variations in ionic radii and electronegativity, which significantly impact the bonding environment and structural stability of the perovskite lattice. Moreover, as the temperature decreased, the sharpening of the C-H alkane and N^+-H bending bands further supported the hypothesized reduced thermal vibrations, suggesting an increased rigidity of the distorted lattice at lower temperatures.[23]

2.2. Investigation of Morphological and Magnetic Properties

The transmission electron microscopy (TEM) images presented in **Figure 3**a–c depict densely packed NCs of CoIn, CoBi, and CoSb, respectively. The NCs exhibited a primarily quasi-spherical or hexagonal faceted morphology, with an average particle size of 39.93 nm for CoIn. In contrast, the average particle size decreased to 18.9 nm for CoBi, while CoSb NCs displayed a significant increase in size compared to the CoIn case, averaging 82.2 nm. High-resolution TEM (HRTEM) images (Figure 3d–f) confirmed the well-defined crystalline nature of all three compositions. Furthermore, compositional analysis using STEM-EDS reconfirmed the expected stoichiometric ratio of Cs:Co:M(III):Cl as 4:1:2:12 across all three $Cs_4CoM(III)_2Cl_{12}$ NC systems. The elemental weight percentages and corresponding EDS spectra for the CoIn, CoBi, and CoSb NCs are provided in Figure S8, Supporting Information, corroborating the compositional accuracy of the synthesized NCs. The measured lattice *d*-spacing values revealed structural variations: for CoIn, a *d*-spacing of 4.12 Å corresponds to the $(11\bar{3})$ lattice plane, whereas in CoBi, the spacing decreased to 3.06 Å, attributed to the $(22\bar{3})$ lattice plane. The CoSb NCs exhibited distinct lattice fringes with expanded *d*-spacing values of 5.3 and 6.4 Å, corresponding to the $(11\bar{2})$ and $(11\bar{1})$ planes, respectively. The change in lattice *d*-spacing indicated the structural distortions that are induced by interlayer stacking and octahedral tilting in the layered perovskite framework. These distortions may also arise due to the ionic size variations of In, Bi, and Sb, leading to lattice contraction or expansion. Additionally, an HRTEM image of CoSb revealed an enlarged lattice *d*-spacing of 10.7 Å, associated with the (001) plane (see Figure S9, Supporting Information). This observation verified the presence of a layered halide perovskite structure, where the trilayer of octahedra is stacked between two adjacent vacancy-ordered layers. Our Fast Fourier Transform (FFT)

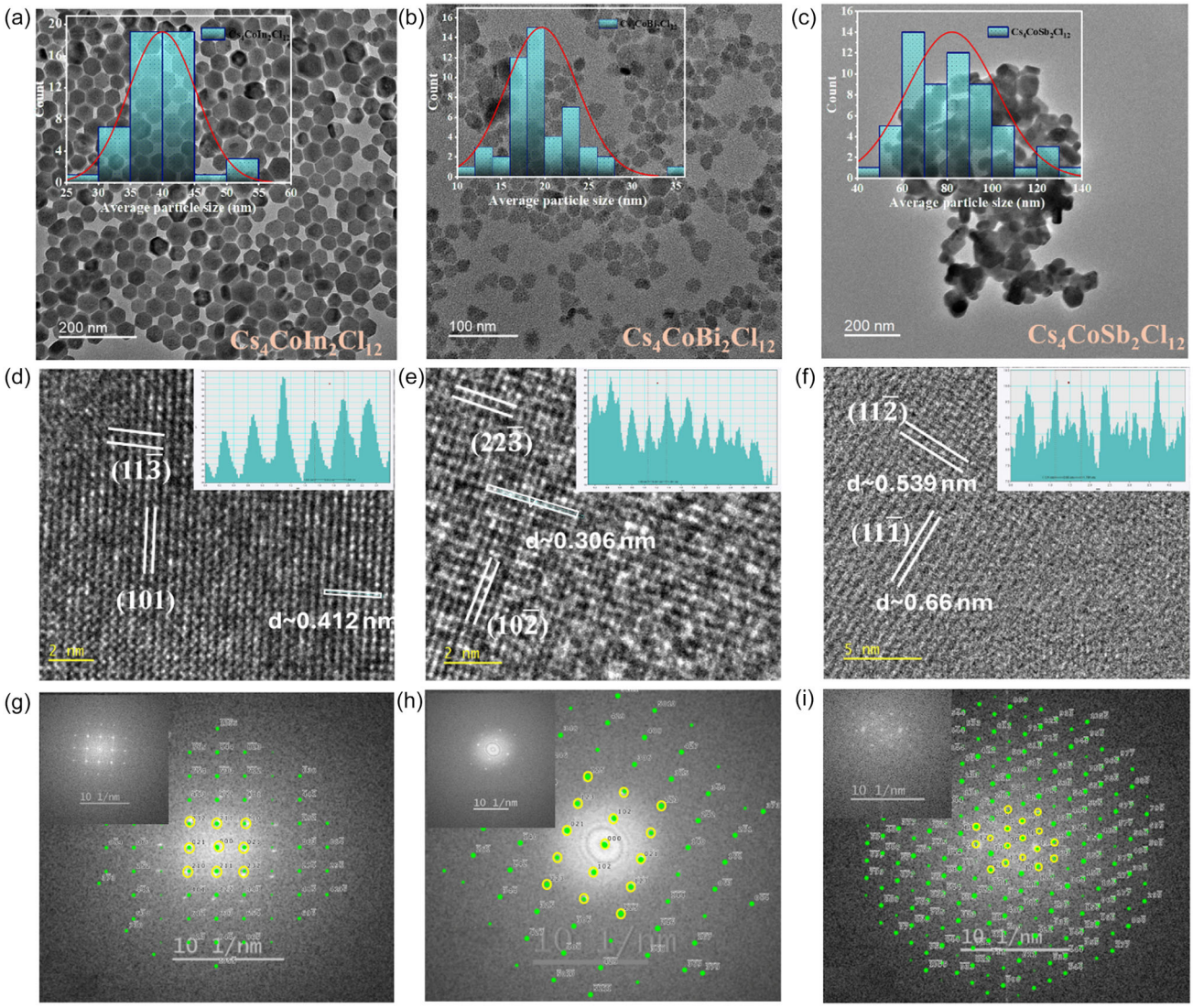

Figure 3. TEM images and size distribution histograms of a) CoIn NCs, b) CoBi NCs, and c) CoSb NCs. HRTEM images with lattice spacing histograms for d) CoIn NCs, e) CoBi NCs, and f) CoSb NCs. g–i) FFT patterns of the as-synthesized NCs overlapped with corresponding simulated structural patterns for CoIn, CoBi, and CoSb NCs, respectively.

analysis, shown in Figure 3g–i, further validates the lattice plane assignments by comparing the HRTEM images with simulated electron diffraction patterns of individual NCs. The simulated patterns align well with experimentally observed FFT data, with viewing zone axes identified as $(\bar{1}\,\bar{1}\,\bar{3})$ for CoIn, $(31\bar{2})$ for CoBi, and (011) for CoSb. The inset images represent the original FFTs of different NC systems, confirming the crystal plane assignments and viewing directions based on the FFT patterns that were obtained from HRTEM analysis.[20]

To further investigate the magnetic properties of the NCs, THz-EPR spectra of CoSb NCs were recorded at 5 K within a range of 5–30 cm^{-1} (Figure S10, Supporting Information). Like the X-band spectra, two distinct species are detected, that are well resolved due to the higher applied magnetic field and corresponding higher excitation frequency. The first resonance appears at 6 T with a frequency of 11 cm^{-1}, while the second, relatively weaker, signal emerges at 7 T and is centered around 18 cm^{-1}. The signals shift toward higher transition energies as the applied magnetic field increases due to the electron Zeeman interaction. To quantitatively analyze the spectra, numerical simulations were performed, also considering the X-band data (Figure 2f). The simulated spectra shown in Figure 2f and S10, Supporting Information, reveal that both the X-band and THz-EPR spectra of CoSb NCs can be well reproduced using the same set of parameters (see Table S3, Supporting Information, for the best-fit parameters). The results further indicate for all investigated NCs that the spectra consist of two HS Co(II) species: a minor species with effective $g'_{\perp}, g'_{||}$ values of approximately [5.0, 2.2] and a major species with approximately [3.5, 2.0] (c.f. Table S3, Supporting Information). Additionally, LS Co(II) in CoIn NCs was best simulated with a g tensor of [2.75, 2.45, 2.4], comprising ≈6% of the total Co(II)

population. However, due to the typically narrower linewidth of $S = 1/2$ systems, the signal exhibits a relatively high amplitude. Note that to reproduce the HS spectra, a rather large line width had to be used. This is tentatively attributed to dipolar and exchange coupling, which is expected between neighboring Co centers. Notably, antisymmetric exchange is often observed in solid-state lattices of coupled magnetic ions[41,42] and could also contribute here due to the lack of inversion symmetry between two neighboring Co atoms. Overall, the above discussion reveals that the magnetic properties of all NCs are governed by the presence of two distinct HS Co(II) species. The observed spectral features suggest significant ZFS and are indicative of complex magnetic coupling within the lattice (detailed discussion included in SI).

2.3. Structural and Compositional Stability in Air

The structural integrity and environmental stability of perovskite NCs are crucial for their practical use and long-term operational performance. To assess their compositional and optical stability, the absorption spectra (**Figure 4**a–c) of fresh and aged perovskite NCs (dispersed in hexane) were recorded upon storage in ambient conditions. In the meanwhile, the XRD patterns versus storage time (Figure 4d–f) were monitored to examine their crystallographic evolution. Figure 4a–c illustrates the long-term optical stability of the $Cs_4CoM(III)_2Cl_{12}$ NCs over a storage period of more than 100 days in ambient conditions. For $Cs_4CoIn_2Cl_{12}$ NCs, a slight red shift in the absorption onsets was observed after 80 days, followed by a notable decrease in the absorbance after 120 days, indicating progressive degradation of the NCs. Similarly, $Cs_4CoBi_2Cl_{12}$ NCs also exhibited a gradual reduction in absorbance at the excitonic peaks or bands with storage time, while the spectral features and peak positions remained largely preserved even after 120 days. This suggests moderate optical stability and slight structural degradation under ambient conditions for both CoIn and CoBi NCs. On the other hand, $Cs_4CoSb_2Cl_{12}$ NCs show a more pronounced decline in absorbance; however, the excitonic peak positions remained almost unchanged. Overall, all three NC systems experienced optical degradation to variable extents, possibly due to storage time-dependent partial decomposition into other by-products (see the XRD stability analysis in the following section), while $Cs_4CoBi_2Cl_{12}$ and $Cs_4CoSbCl_{12}$ NCs demonstrated relatively better spectral retention despite reduced absorbance, which compromises the light absorption efficiency. Nevertheless, compared to traditional lead-based perovskite NCs, the overall optical stability of these lead-free NCs remains relatively high, particularly with CoSb, which achieved the highest resilience.[43,44]

To monitor the structural changes in LDP NCs over time, the thin films of NCs were prepared and stored under ambient conditions (25 °C and ≈60% humidity), and their XRD patterns were recorded periodically. It is noted that the CoIn NC film can retain its crystalline structure for up to 40 days, as evidenced by the persistence of sharp diffraction peaks. However, after 40 days, peak broadening and a reduction in peak intensity were also observed, signifying the onset of structural degradation; a similar situation was observed for the CoBi NC film. For the CoIn films, we observed that the degradation becomes prominent after 40 days of ambient storage. The original perovskite phase gradually decomposes, and the resulting XRD pattern of the aged sample

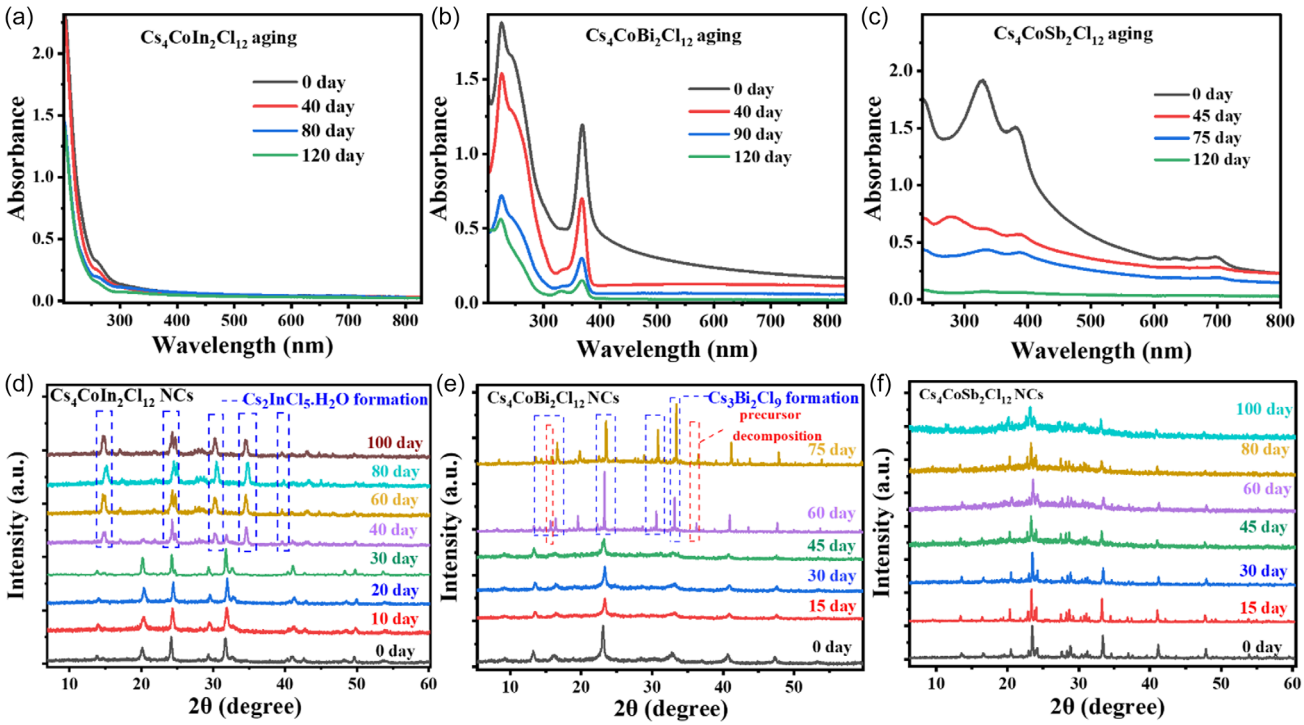

Figure 4. Long-term stability analysis: UV absorption spectra of a) CoIn, b) CoBi, and c) CoSb NCs over 100 days of storage in air. Evolution of normalized XRD patterns for d) CoIn, e) CoBi, and f) CoSb NCs.

exhibits new peaks that match well with the known single-crystal XRD pattern of $Cs_2InCl_5{\cdot}H_2O$.[45] This suggests a hydrolysis of the indium-containing perovskite component, likely due to moisture-induced degradation. Minor additional peaks are also attributed to by-products of the decomposition, such as $CoCl_2$ and $InCl_3$, further confirming the degradation pathway. In the case of $Cs_4CoBi_2Cl_{12}$, the degradation was found to be initiated after ≈45 days of storage. The XRD patterns of the aged film reveal the emergence of new reflections consistent with the relatively thermodynamically stable $Cs_3Bi_2Cl_9$ phase.[46] This transition plausibly results from phase segregation and structural rearrangement under ambient conditions. Figure S11, Supporting Information, confirms these assignments through XRD pattern matching of both experimental and simulated references by comparing the fresh and aged XRD patterns alongside the relevant references. On the contrary, the CoSb NC film demonstrated significantly enhanced air stability, with their characteristic diffraction peaks remaining intact for over 100 days postsynthesis. Only a minor decrease in peak intensity was observed without the emergence of additional diffraction peaks, suggesting that the CoSb NC films indeed exhibit enhanced structural stability in ambient conditions. Additionally, the EDS measurements were performed again on the same hexane-dispersed NC suspensions for all three samples after 120 days postsynthesis to assess their compositional stability. The results indicate that the elemental stoichiometry remained largely consistent, exhibiting only minor deviations from the initial composition measured on day 1. These findings further suggest that the NCs can effectively retain their desired chemical composition over an extended period in the solution phase. The detailed elemental mapping and compositional analysis are provided in Figure S12, Supporting Information, and Table S4, Supporting Information. Conclusively, our comprehensive stability analysis reveals that the CoSb NCs feature better structural and optical stability compared to other CoIn and CoBi counterparts. More importantly, the elemental composition of all NCs remains unchanged after 120 days of storage in solution, highlighting their overall high operational stability as promising candidates for long-term optoelectronic and photocatalytic applications.

2.4. Photoelectrochemical Activity

The PEC technique serves as a versatile and sensitive method for investigating the intrinsic physical and chemical characteristics of metal halide perovskite,[47] which has inspired us to explore the potential of newly synthesized LDP NCs for PEC applications such as PEC oxidation of organic compounds (e.g., benzoquinone). The cyclic voltammetry (CV) was first used to determine the valence and conduction bands of as-synthesized NCs. The detailed CV setup is described in the Experimental Section and Figure S13a (CV of the F_c/F_c^+ standard) in the Supporting Information. Figure S13b, Supporting Information, presents the resulting CV profiles for the series of NCs. The oxidation peak potentials were observed at 1.68 V for CoIn, while CoBi and CoSb exhibited peak shifts to 1.59 and 1.05 V, respectively. Using the Fc/Fc^+ reference energy level of 4.8 eV versus vacuum, the valence and conduction band positions were calculated using $E_{VB} = -(V_{ox} - V(Fc/Fc^+) + 4.8)$ eV and $E_{CB} = E_{VB} + E_g$ equations, where $V(Fc/Fc^+)$ is the midpotential of ferrocene standard and E_g is the optical bandgap of perovskite NCs calculated from the Tauc plot analysis. The CoIn NCs demonstrated valence and conduction band energies of −6.02 and −2.35 eV, respectively; CoBi exhibited −5.93 and −2.70 eV, respectively, while CoSb showed values of −5.39 and −2.51 eV for valence band and conduction band energy levels.[48] The corresponding energy-level diagrams for these NCs were compared in Figure S13c, Supporting Information, all of which are suitable for potentially realizing a PEC redox reaction (e.g., redox potential of water splitting >1.23 eV).[49] Consequently, the PEC measurements were conducted using a standard three-electrode system (see the inset schematic in **Figure 5**a) under 1 Sun illumination (100 mW cm^{-2}). The electrolyte solution was prepared by dissolving 0.1 M tetrabutylammonium hexafluorophosphate ($TBAPF_6$) and 4 mM benzoquinone in anhydrous dichloromethane (DCM). In this system, $TBAPF_6$ acted as a supporting electrolyte to improve ionic conductivity, while benzoquinone served as a redox mediator to facilitate photohole capture from the perovskite NCs-based photoanode.[50] The solvent stability of the NC films was evaluated by immersing them in various solvents, including propanol, ethanol, and DCM. The XRD analysis revealed that all NC films can retain their structural integrity after prolonged exposure to DCM, whereas noticeable structural degradation or changes were observed in other solvents (Figure S14, Supporting Information). Upon illumination, the NCs working electrode generated charge carriers, thereby enabling photoexcited holes to oxidize benzoquinone into various potential products, including benzoquinone cation radical ($C_6H_4O_2{\bullet}^+$) or hydroxylated benzoquinone derivatives. The photoexcited electrons in the process are transferred to the FTO substrate via an n-type TiO_2 compact layer under an applied potential of +1.0 V versus Ag/AgCl, thereby completing the redox cycle at the counter electrode (Pt) for the complete PEC reaction.[51] Among the tested NC photoelectrodes, CoSb and CoBi NCs demonstrated significantly enhanced photocurrent densities compared to the CoIn NCs, with improvements observed in both transient and steady-state regimes. Notably, the optimized CoBi-based electrode achieved the highest photocurrent density, reaching 150 μA cm^{-2} at around 1.6 V, corresponding to a 1.5-fold increase relative to the CoIn case (Figure 5a). These findings underscore the superior PEC performance of CoBi NCs and their potential for high-performance PEC applications. As illustrated in Figure 5b, the amperometric J–t curves recorded at a potential of 1.0 V versus Ag/AgCl exhibited consistent and reproducible photocurrent responses under repeated light on/off cycles, highlighting the high stability of the LDP NC-based photoelectrodes. The CoBi NCs exhibited the highest on/off ratio of 145.78, surpassing those of CoSb and CoIn NCs, which were calculated as 32.22 and 20.56, respectively. The elevated on/off ratio observed for CoBi NCs signifies its enhanced photoresponse sensitivity, efficient charge carrier transport at the photoelectrode, and reduced dark current leakage. Regarding the differences in photocurrent peak shapes observed in Figure 5b, these variations can be attributed to differences in the intrinsic optoelectronic properties of the respective NCs, possibly including two major factors: *(i)* Differences in charge mobility among CoIn, CoSb, and CoBi could affect how quickly electrons and holes are collected at electrodes; thus, NCs with higher mobility may lead to faster stabilization of photocurrent under illumination, which shows

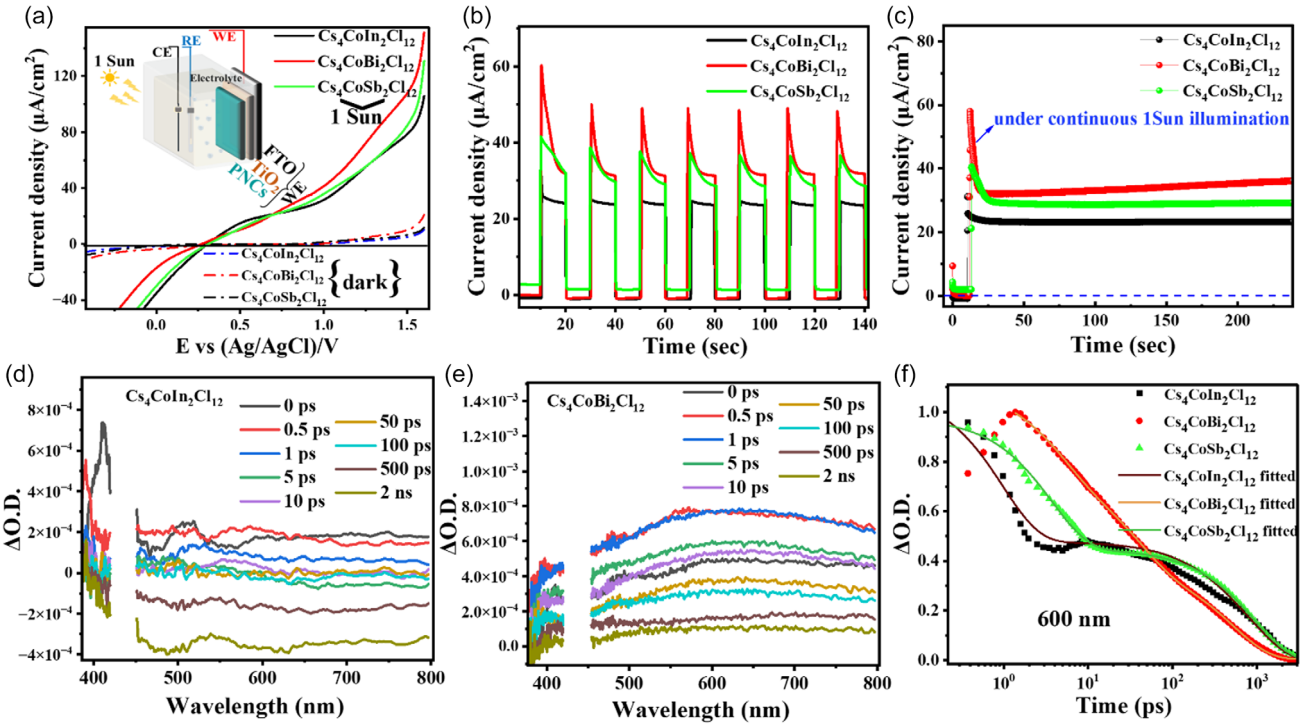

Figure 5. a) Current density versus applied potential (vs. Ag/AgCl) of $Cs_4CoM(III)_2Cl_{12}$ NCs-based photoelectrodes recorded in the dark and under 1 Sun illumination (AM 1.5 G, 100 mW cm^{-2}). The potential was systematically varied from +1.6 to –0.6 V versus Ag/AgCl. The active electrode area in contact with the electrolyte during measurements is 2.01 cm^2. b) Amperometric photocurrent density curves for $Cs_4CoM(III)_2Cl_{12}$ NCs under repeatable light ON/OFF conditions. c) Time-dependent photocurrent density decay curves recorded for $Cs_4CoM(III)_2Cl_{12}$ NCs under continuous 1 Sun illumination. Ultrafast transient absorption spectra of d) CoIn and e) CoBi NCs suspensions in hexane, excited at 266 nm. f) TA decays of three NCs suspensions monitored at peaks (410 nm for CoIn and CoSb NCs, 600 nm for CoBi NCs) of PIA bands, respectively.

a desired order of CoBi > CoSb > CoIn. *(ii)* Slower decay of the peak photocurrent (the CoIn case) suggests a higher density of trap states or surface defects that momentarily store charge carriers and release them over time in a nonradiative way by lowering the photocurrent density, compared to CoBi and CoSb cases, which are also supported by our transient absorption analysis in the following section. Moreover, the conduction band of CoBi NCs (−2.70 eV) is positioned lower than that of CoIn (−2.35 eV) and CoSb (−2.51 eV) (see Figure S13c, Supporting Information), which is closer to the conduction band (−4.2 eV) of TiO_2 buffer layer, thereby being more favorable for efficient electron transfer that is beneficial for overall high PEC performance upon the FTO/TiO_2/CoBi NCs configuration.

Figure 5c represents the photocurrent decay of these NC-based PEC cells under continuous 1 Sun illumination. The CoBi NC-based cell exhibited the highest initial photocurrent density (60 μA cm^{-2}) and maintained the largest steady-state photocurrent, whereas the CoSb cell demonstrated moderate performance with initial and steady-state photocurrents lower than the CoBi one but higher than the case of CoIn NCs. However, all the NC-based photoelectrodes presented highly stable photocurrent plateaus after the fast initial decay, reflecting their PEC stability under prolonged illumination. A comparative analysis of the electrochemical performance of the as-synthesized NCs with other benchmark lead-free NCs and photochemical systems is provided in Table S5, Supporting Information. It is noted that the PEC performance of CoM(III) NCs in this work has outperformed most of the reported lead-free perovskite-based PEC systems, even comparable with those conventional and commercialized metal oxide systems, which underscores the potential use of these lead-free LDP NCs as promising photoelectrode materials. We further conducted electrochemical impedance spectroscopy (EIS) measurements for the CoBi and CoIn NCs to elucidate the charge transfer properties. The corresponding Nyquist plots for all three NC systems are presented in Figure S15, Supporting Information, where the obtained semicircles were modeled using a simplified RC equivalent circuit. The series (R_s) and charge transport resistance (R_{ct}) were determined under both dark and 1 Sun illumination conditions. A substantial reduction in series resistance (R_s) values was observed upon illumination for both NC systems, with CoBi exhibiting the lowest Rs value of 1384 Ω among all, indicating superior charge transfer efficiency. Likewise, the Rct value significantly decreased under illumination, dropping from 14 850 Ω (dark) to 5,146 Ω (light) for CoBi. This reduction in R_{ct} under light exposure suggests enhanced charge carrier mobility and more efficient charge separation within the photoelectrode.[52] Table S6, Supporting Information, summarizes the fitted values of R_s and R_{ct} as well as other corresponding parameters of EIS analysis.

To gain more insight into the correlation between photophysical properties and PEC performance, we conducted the ultrafast

transient absorption (TA) measurements for CoM(III) LDP NCs in suspension, as shown in Figure 5d–e for CoIn and CoBi, respectively, and in Figure S16, Supporting Information for CoSb. All NC suspensions were excited at 266 nm with an excitation power range of 0.4–1.4 mW. A broad and positive photoinduced absorption (PIA) ranging from 380 nm to around 800 nm (limitation of our visible detector) was clearly detected only in the case of CoBi NCs, while both CoIn and CoSb NCs exhibited relatively weak and tilted PIA signals between 380 and ≈450 nm. This suggests that more STE states can be formed in the $[BiCl_6]$-$[CoCl_6]$-$[BiCl_6]$ layered structure rather than the other two cases, that is, $[InCl_6]$ or $[SbCl_6]$ octahedra. The ultrafast PIA signal growth (<1.5 ps) indicates a transition from free excitons to STEs trapping.[53] The observed large redshift in the TA spectra of CoBi NCs compared to those spectra of CoIn and CoSb NCs (see Figure S17, Supporting Information), particularly after 2 ps, confirms a strengthened STE effect upon the coordination of $[BiCl_6]$ octahedra in the layered structure. Furthermore, the TA decays of three NCs were compared in Figure 5f and monitored at their respective peaks of PIA bands. A tri-exponential function was employed to fit all three TA decays well; the fitting results are summarized in Table S7, Supporting Information. We assigned two fast processes consisting of an ultrafast component and a middle-fast component to nonradiative transitions and a slow component to radiative recombination of STEs.[22] To simplify the comparison of fitted decay lifetimes, we extracted the half-lifetime, $\tau_{1/2}$, in each case, that is, 3.1 ps for CoIn, 8.3 ps for CoSb, and 34.2 ps for CoBi, indicating that $[BiCl_6]$ octahedral coordination could induce more Jahn–Teller distortion in common $[CoCl_6]$ octahedra, which eventually leads to more radiative transition of STE states rather than the dominant dark transition (with shorter half-lifetimes) in both cases of $[InCl_6]$ and $[SbCl_6]$ octahedra. This prolonged TA decay lifetime of CoBi NCs is, in turn, beneficial for efficient charge transfer, particularly at the interface of CoBi NCs and electrolyte (benzoquinone), by achieving high photogenerated current density as observed previously.

3. Conclusion

In summary, we have successfully tailored the M(III) site cation substitution in $Cs_4CoM(III)_2Cl_{12}$ LDPs through a facile colloidal synthesis, enabling the precise tuning of bandgap and charge transfer properties in this first-ever class of NCs. A comprehensive study of M(III) site-induced change in optoelectronic properties and compositional stability of the as-synthesized $Cs_4CoM(III)_2Cl_{12}$ NCs has been conducted upon the establishment of a direct composition-structure–property relationship. Benefiting from the featured LDP structure, all $Cs_4CoM(III)_2Cl_{12}$ NCs exhibit relatively high structural stability after long-time storage in the ambient atmosphere. In addition, our findings reveal that variations in the M(III) cation significantly impact the PEC behavior of all three NC-based photoelectrode systems. Notably, $Cs_4CoBi_2Cl_{12}$ LDP NCs exhibit exceptional potential for PEC applications by showing a moderately high photocurrent density of ≈150 μA cm^{-2} at 1.6 V versus Ag/AgCl, which represents a relatively high photocurrent density compared to most lead-free perovskites or perovskite-inspired materials-based PEC systems. We thus believe that this work will assist in pushing the development of lead-free perovskite nanomaterials for further PEC and optoelectronic applications.

Supporting Information

Supporting Information is available from the Wiley Online Library or from the author.

Acknowledgements

M.L. and Yukta acknowledge the Royal Physiographic Society of Lund and Crafoord Foundation (No. 20240745) for funding. This work was partially supported by the Wallenberg Initiative Materials Science for Sustainability (WISE), funded by the Knut and Alice Wallenberg Foundation. The authors acknowledge the Swedish Research Council and SSF for access to nCHREM, which is a part of ARTEMI, the Swedish National Infrastructure in Advanced Electron Microscopy (2021-00171 and RIF21-0026). T.A.S., A.O.B., and K.R. thank Helmholtz-Zentrum Berlin for the allocation of instrument time at the THz beamline at BESSY II (Proposal number 242-12743-ST) and the Energy Materials In-situ Laboratory (EMIL) operated by HZB for granting access to its chemistry laboratory. This work was partially funded by the Deutsche Forschungsgemeinschaft (DFG, German Research Foundation) under Germany's Excellence Strategy—EXC 2008-390540038—UniSysCat to K.R., and A.O.B. thanks Einstein Foundation Berlin (ESB)—Einstein Center of Catalysis (EC2) for their scholarship and support. Q.S. and T.P. would like to acknowledge financial support from the Swedish Energy Agency, the Swedish Research Council, WISE, WASP, and the LU profile area Light and Materials. We acknowledge the MAX IV Laboratory for beamtime on the FinEstBeAMS beamline under proposal (proposal ID: 20241059). Research conducted at MAX IV, a Swedish national user facility, is supported by Vetenskapsrådet (Swedish Research Council, VR) under contract 2018-07152, Vinnova (Swedish Governmental Agency for Innovation Systems) under contract 2018-04969 and Formas under contract 2019-02496. [Correction added on 10 September 2025 after online publication: The acknowledgement was corrected in this version.]

Conflict of Interest

The authors declare no conflict of interest.

Data Availability Statement

The data that support the findings of this study are available from the corresponding author upon reasonable request.

Keywords

colloidal nanocrystals, lead-free layered double perovskites, photoelectrochemical reactions, self-trapped excitons, structural engineering

Received: March 23, 2025
Revised: June 2, 2025
Published online: June 29, 2025

[1] X. Ling, S. Zhou, J. Yuan, J. Shi, Y. Qian, B. W. Larson, Q. Zhao, C. Qin, F. Li, G. Shi, C. Stewart, J. Hu, X. Zhang, J. M. Luther, S. Duhm, W. Ma, *Adv. Energy Mater.* **2019**, *9*, 1900721.

[2] H. Yang, Y. Zhang, K. Hills-Kimball, Y. Zhou, O. Chen, *Sustainable Energy Fuels* **2018**, *2*, 2381.
[3] J. Ye, M. M. Byranvand, C. O. Martínez, R. L. Z. Hoye, M. Saliba, L. Polavarapu, *Angew. Chem. Int. Ed.* **2021**, *60*, 21636.
[4] F. Yan, S. T. Tan, X. Li, H. V. Demir, *Small* **2019**, *15*, 1902079.
[5] D. Han, M. Imran, M. Zhang, S. Chang, X. G. Wu, X. Zhang, J. Tang, M. Wang, S. Ali, X. Li, G. Yu, J. Han, L. Wang, B. Zou, H. Zhong, *ACS Nano* **2018**, *12*, 8808.
[6] C. H. Chen, S. N. Cheng, L. Cheng, Z. K. Wang, L. S. Liao, *Adv. Energy Mater.* **2023**, *13*, 2204144.
[7] M. Ren, X. Qian, Y. Chen, T. Wang, Y. Zhao, *J. Hazard. Mater.* **2022**, *426*, 127848.
[8] F. Giustino, H. J. Snaith, *ACS Energy Lett.* **2016**, *1*, 1233.
[9] Q. Fan, G. V. Biesold-McGee, J. Ma, Q. Xu, S. Pan, J. Peng, Z. Lin, *Angew. Chem.* **2020**, *132*, 1042.
[10] Z. Xiao, Z. Song, Y. Yan, *Adv. Mater.* **2019**, *31*, 1803792.
[11] Z. Liu, J. Zito, M. Ghini, L. Goldoni, M. Prato, H. Bahmani Jalali, I. Infante, L. De Trizio, L. Manna, *Nano Lett.* **2022**, *22*, 8567.
[12] S. A. U. Hasan, D. S. Lee, S. H. Im, K. H. Hong, *Solar RRL* **2020**, *4*, 1900310.
[13] B. Al-Anesi, G. K. Grandhi, A. Pecoraro, V. Sugathan, N. S. M. Viswanath, H. Ali-Löytty, M. Liu, T. P. Ruoko, K. Lahtonen, D. Manna, S. Toikkonen, A. B. Muñoz-García, M. Pavone, P. Vivo, *Small* **2023**, *19*, 2303575.
[14] B. Saparov, D. B. Mitzi, *Chem. Rev.* **2016**, *116*, 4558.
[15] B. Vargas, G. RodrÍguez-López, D. Solis-Ibarra, *ACS Energy Lett.* **2020**, *5*, 3591.
[16] B. Vargas, E. Ramos, E. Pérez-Gutiérrez, J. C. Alonso, D. Solis-Ibarra, *J. Am. Chem. Soc.* **2017**, *139*, 9116.
[17] G. Volonakis, M. R. Filip, A. A. Haghighirad, N. Sakai, B. Wenger, H. J. Snaith, F. Giustino, *J. Phys. Chem. Lett.* **2016**, *7*, 1254.
[18] B. Vargas, R. Torres-Cadena, D. T. Reyes-Castillo, J. Rodríguez-Hernández, M. Gembicky, E. Menéndez-Proupin, D. Solis-Ibarra, *Chem. Mater.* **2020**, *32*, 424.
[19] Y. P. Lin, S. Hu, B. Xia, K. Q. Fan, L. K. Gong, J. T. Kong, X. Y. Huang, Z. Xiao, K. Z. Du, *J. Phys. Chem. Lett.* **2019**, *10*, 5219.
[20] T. Cai, W. Shi, S. Hwang, K. Kobbekaduwa, Y. Nagaoka, H. Yang, K. Hills-Kimball, H. Zhu, J. Wang, Z. Wang, Y. Liu, D. Su, J. Gao, O. Chen, *J. Am. Chem. Soc.* **2020**, *142*, 11927.
[21] Y. Wang, Y. Ji, Y. Yang, Z. Chen, H. Sun, X. Wang, Z. Zou, H. Huang, *ACS Energy Lett.* **2024**, *9*, 336.
[22] M. Liu, S. K. Matta, H. Ali-Löytty, A. Matuhina, G. K. Grandhi, K. Lahtonen, S. P. Russo, P. Vivo, *Nano Lett.* **2022**, *22*, 311.
[23] H. Mai, X. Li, J. Lu, X. Wen, T. C. Le, S. P. Russo, D. Chen, R. A. Caruso, *J. Am. Chem. Soc.* **2023**, *145*, 17337.
[24] M. Liu, S. K. Matta, T. Al Said, J. Liu, A. Matuhina, B. Al-Anesi, H. Ali-Löytty, K. Lahtonen, S. P. Russo, P. Vivo, *Small* **2024**, *20*, 2401051.
[25] W. Ning, F. Gao, *Adv. Mater.* **2019**, *31*, 1900326.
[26] M. Uchikoshi, *J. Sol. Chem.* **2018**, *47*, 2021.
[27] P. R. Jubu, O. S. Obaseki, D. I. Ajayi, E. Danladi, K. M. Chahrour, A. Muhammad, S. Landi, T. Igbawua, H. F. Chahul, F. K. Yam, *J. Opt.* **2024**, *53*, 5054.
[28] T. Appadurai, S. Chaure, M. Mala, A. K. Chandiran, *Energy and Fuels* **2021**, *35*, 11479.
[29] S. Wang, Y. Xie, M. Zhao, J. Sun, W. Wu, Z. Liu, H. Sun, L. Lu, K. Shi, L. Qi, K. Pan, *J. Alloys. Compd.* **2024**, *1003*, 175652.
[30] J. Im, C. C. Stoumpos, H. Jin, A. J. Freeman, M. G. Kanatzidis, *J. Phys. Chem. Lett.* **2015**, *6*, 3503.
[31] D. Phelan, D. Louca, K. Kamazawa, M. F. Hundley, K. Yamada, *Phys. Rev. B* **2007**, *76*, 104111.
[32] C. Wang, M. Sun, H. Wang, G. Zhao, *J. Phys. Chem. Lett.* **2023**, *14*, 164.
[33] J. Tan, D. Li, J. Zhu, N. Han, Y. Gong, Y. Zhang, *Nanoscale* **2022**, *14*, 16394.
[34] M. D. Smith, H. I. Karunadasa, *Acc. Chem. Res.* **2018**, *51*, 619.
[35] R. Song, S. Xu, Y. Li, Q. Zhang, Y. Gao, H. Yu, Y. Cao, X. Li, S. Zhang, B. Chen, *Spectrochim. Acta A Mol. Biomol. Spectrosc.* **2023**, *288*, 122181.
[36] F. M. Rombach, L. Gregori, A. Sidler, J. Whitworth, S. Zeiske, H. Jin, E. Y. H. Hung, S. Motti, P. Caprioglio, A. Armin, M. Lenz, D. Meggiolaro, F. De Angelis, H. J. Snaith, *J. Mater. Chem. C* **2025**, *13*, 5161.
[37] J. Cañón, A. V. Teplyakov, *Surf. Interface Anal.* **2021**, *53*, 475.
[38] M. W. Makinen, L. C. Kuo, M. B. Yim, G. B. Wells, J. M. Fukuyama, J. E. Kim, *J. Am. Chem. Soc.* **1985**, *107*, 5245.
[39] S. Mourdikoudis, M. Menelaou, N. Fiuza-Maneiro, G. Zheng, S. Wei, J. Pérez-Juste, L. Polavarapu, Z. Sofer, *Nanoscale Horiz.* **2022**, *7*, 941.
[40] J. Ibarra, J. Melendres, M. Almada, M. G. Burboa, P. Taboada, J. Juárez, M. A. Valdez, *Mater. Res. Express.* **2015**, *2*, 095010.
[41] D. Coffey, K. S. Bedell, S. A. Trugman, *Phys. Rev. B* **1990**, *42*, 6509.
[42] J. S. Zhou, L. G. Marshall, Z. Y. Li, X. Li, J. M. He, *Phys. Rev. B* **2020**, *102*, 104420.
[43] J. C. Dahl, W. T. Osowiecki, Y. Cai, J. K. Swabeck, Y. Bekenstein, M. Asta, E. M. Chan, A. P. Alivisatos, *Chem. Mater.* **2019**, *31*, 3134.
[44] B. Luo, Y. Pu, S. A. Lindley, Y. Yang, L. Lu, Y. Li, X. Li, J. Z. Zhang, *Angew. Chem* **2016**, *128*, 9010.
[45] P. Han, C. Luo, S. Yang, Y. Yang, W. Deng, K. Han, *Angew. Chem. Int. Ed.* **2020**, *59*, 12709.
[46] E. E. Morgan, L. Mao, S. M. L. Teicher, G. Wu, R. Seshadri, *Inorg. Chem.* **2020**, *59*, 3387.
[47] K. Bienkowski, R. Solarska, L. Trinh, J. Widera-Kalinowska, B. Al-Anesi, M. Liu, G. K. Grandhi, P. Vivo, B. Oral, B. Yılmaz, R. Yıldırım, *ACS Catal.* **2024**, *14*, 6603.
[48] M. Liu, G. Krishnamurthy Grandhi, B. Al-Anesi, H. Ali-Löytty, K. Lahtonen, R. Grisorio, P. Vivo, *Electrochim. Acta* **2023**, *462*, 142734.
[49] H. Idriss, *Catal. Sci. Technol.* **2020**, *10*, 304.
[50] M. Z. Yang, Y. F. Xu, J. F. Liao, X. D. Wang, H. Y. Chen, D. Bin Kuang, *J. Mater. Chem. A* **2019**, *7*, 5409.
[51] L. K. M. Lam, Z. Zhang, P. G. Board, L. Xun, *Biochemistry* **2012**, *51*, 5014.
[52] Yukta, R. D. Chavan, A. Mahapatra, D. Prochowicz, P. Yadav, P. K. Iyer, S. Satapathi, *ACS Appl. Mater. Interfaces* **2023**, *15*, 53351.
[53] T. Hu, M. D. Smith, E. R. Dohner, M. J. Sher, X. Wu, M. T. Trinh, A. Fisher, J. Corbett, X. Y. Zhu, H. I. Karunadasa, A. M. Lindenberg, *J. Phys. Chem. Lett.* **2016**, *7*, 2258.